

Folded monocentric imager with deformable mirror focus

GLENN M. SCHUSTER,* WILLIAM M. MELLETTE, AND JOSEPH E. FORD

Department of Electrical & Computer Engineering, University of California San Diego, 9500 Gilman Drive, La Jolla, California 92093, USA

*Corresponding author: gschuster@eng.ucsd.edu

Received 13 February 2017; revised 22 March 2017; accepted 23 March 2017; posted 24 March 2017 (Doc. ID 286353); published 17 April 2017

We describe a catadioptric monocentric imager using an elastic central element focused by deformation of a fold mirror. We show the design of 6 mm and 12 mm focal length F/2.8 achromats and compare design performance when focusing by translating the sensor, translating the fold mirror, and by spherically deforming the fold mirror. We tested the 12 mm focal length design using a diamond turned polystyrene element as the outer meniscus lens (and mechanical mount), filled with an optical gel in contact with the central aperture and fold mirror, and demonstrate focusing by mechanical deformation of the fold mirror. The resolution at the spherical image surface was inspected by optical relay imaging, yielding a best focus MTF₅₀ of 52.6 lp/mm. © 2017 Optical Society of America

OCIS codes: (110.0110) Imaging systems; (220.0220) Optical design and fabrication; (220.3620) Lens system design; (220.4840) Testing.

<https://doi.org/10.1364/AO.56.003435>

1. INTRODUCTION

Compact imagers with high resolution and wide field-of-view (FOV) must fit into ever smaller packages for use in mobile devices, augmented reality, and consumer photography. Many types of compact imagers have been demonstrated, including deformable liquid under membrane lenses actuated by servo motor pressure on a reservoir [1], iris contraction [2], electromagnetic force [3], and thermal expansion [4]. One compact lens geometry with high resolution over a wide FOV is “monocentric,” where all surfaces share a common center of curvature [5]. The formed spherical image can be captured using one or more fiber-coupled (FC) complementary metal-oxide-semiconductor (CMOS) sensors [6,7]. Figure 1(a) shows the refractive monocentric imager and FC sensors of [6]. These previously demonstrated imagers used a solid glass monocentric lens with a fixed aperture stop at the center and were focused by axial translation of the FC image sensors relative to the lens.

It is possible to introduce a central fold mirror without necessarily breaking the monocentric symmetry. This was done in a refractive monocentric projector [8] and in the catadioptric Bouwers telescope [9,10]. Folding the lens reduces the optical track length and can yield an even more compact wide-angle imager, at the cost of limiting the FOV along the folding (e.g., vertical) axis. Figure 1(b) diagrams a refractive monocentric lens, a layout with an internal fold mirror at the lens center, and another layout that further reduces system volume by adding a second fold mirror between the lens and focal surface. The

refractive monocentric lens is focused by axial translation, but folding provides direct access to the lens aperture stop and enables internal focusing by mirror axial translation or deformation. Both of these focus mechanisms break strict monocentric symmetry, but they can still provide effective focus and reduce the achievable imager system volume. Here we look at three options for focusing a folded monocentric imager, downselect to deformable mirror focus based on the small mechanical excursion needed, and then demonstrate a 12-mm focal length (f) lens using mechanical fold mirror deformation to focus. The paper is organized as follows. In Section 2, we provide the optical design of a two-element folded achromat with an optical gel core and compare three methods of focusing for 6- and 12-mm focal length designs. In Section 3, we discuss options for mirror actuation, comparing them in terms of total mechanical excursion, and experimentally characterize a mirror surface profile under mechanical actuation. In Section 4, we describe the integration and test of a prototype imaging system, showing image acquisition using a FC image sensor. We conclude in Section 5.

2. OPTICAL DESIGN

A. Focusing

Traditional objective lenses are focused by translating the lens relative to the image plane. When a monocentric lens images an object at a constant radial range (a spherical object) onto a spherical image surface, focus is directly analogous to

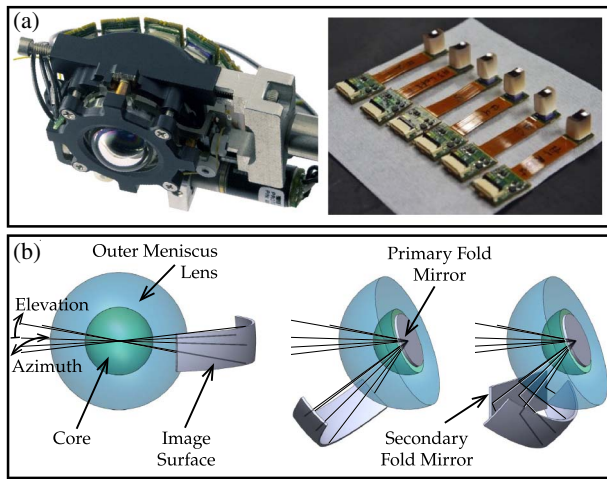


Fig. 1. (a) Photo of the 30 MPixel monocentric “letterbox” format camera and FC sensors described in [6], and (b) perspective conceptual diagrams comparing a refractive monocentric lens, a monocentric lens with a central fold mirror at 22°, and the same lens with a secondary mirror to further reduce the system footprint.

expanding the radius of curvature of the spherical image sensor. This suggests that a fixed-spherical radius sensor can only focus to a single direction at one time. However, for a monocentric lens designed to focus an object at infinity, axially translating the monocentric lens away from the fixed-radius image surface maintains focus for a planar object surface at a closer range, and the planar object remains in sharp focus across the 124° or larger FOV [5]. This method of refocusing requires optomechanics to move the entire lens or sensor assembly while maintaining alignment in the other four spatial and rotational dimensions.

A folded monocentric lens, with a mirror placed at the center of curvature, can apply the same axial translation for focus. However, if the central lens element is not solid, alternative methods can be employed. It is not possible to design a positive focal length monocentric lens with a hollow center, but the central element can be made of an optical liquid or gel. In this case, the planar fold mirror can be translated, or piston shifted, inside the monocentric lens core to add or remove path length within the lens and modify the focus. Alternately, the mirror can be deformed by adding positive or negative spherical curvature (without axial translation of the center of the fold

mirror), which also changes the focus of the lens. Figure 2 shows these three discrete methods. Of course, the same uniform or quadratically varying phase profile could be applied using an optoelectronic phase modulator, such as a reflective liquid crystal on silicon display, but here we restrict our discussion (and experimental demonstration) to physical motion or deformation of the fold mirror.

The internal focus mechanisms reduce the total physical length of motion required to refocus, which can enable smaller or more cost-effective mechanical or optoelectronic focus actuators. Multiple methods can also be combined (e.g., piston shift and mirror deformation) to optimize lens performance and further reduce the travel length. All the internal focus methods break the perfect spherical symmetry of the lens, which tends to reduce resolution. This resolution loss may or may not be critical, depending on how the spherical image is captured. In the monocentric imagers of [6,7], MTF50 resolution was limited by the FC CMOS sensors to some 35 lp/mm before processing and 70 lp/mm after processing, making it worthwhile to explore alternate focus mechanisms.

The solid glass lenses of [6,7] were fabricated with at least four discrete elements. The spherical symmetric central (crown glass) cores were fabricated as two hemispheres, one of which was cut and painted with an optical aperture. The outer (flint glass) elements were fabricated as two meniscus lenses. The four elements were assembled and bonded using conventional methods into a solid focus group. Our proposed folded monocentric lens structure is a two-material symmetric achromat consisting of a single rigid outer meniscus (flint material) lens filled with an optical gel (crown material) in contact with the central aperture stop and fold mirror. This geometry simplifies the required optical fabrication to a single outer meniscus lens element, whose inner radius defines the central element, and also eliminates the adhesive between two more rigid elements. After optimizing the design with a catalog of diamond turnable plastics and viscous optical gels, we chose to use a direct single point diamond turned polystyrene plastic as the outer element for the prototype, with index 1.59 and Abbe number of 30.9. Polystyrene is also compatible with molding for low-cost volume production. The selected inner core material was a standard commercially available optical gel (Cargile 0608) with index 1.46 and Abbe number 55.5.

To allow comparisons to previous glass monocentric lenses and to provide compatibility with the radius of curvature on

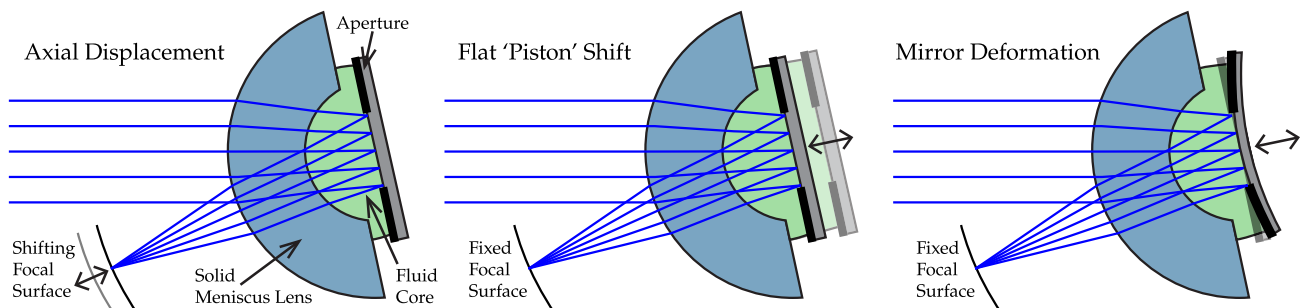


Fig. 2. Conventional axial displacement (left) of focal plane, piston shift (middle) of rigid mirror, and mirror deformation (right) methods of focusing folded monocentric lens.

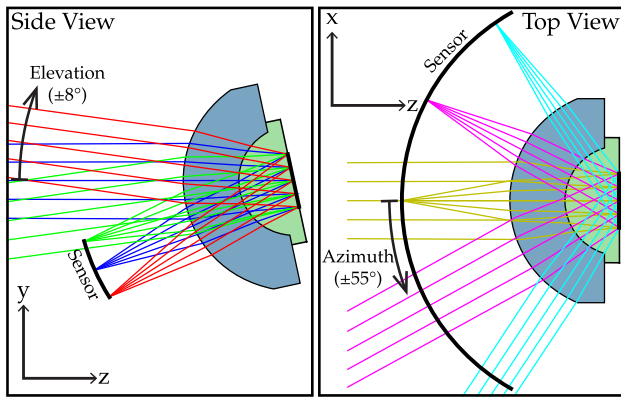


Fig. 3. Side view (left) and top view (right) optical ray trace of the $f = 12$ mm folded monocentric lens with a 12° fold angle, which was chosen to balance the vertical vignetting across the image surface.

our existing FC image sensors, we designed the folded lens with the same 12-mm focal length; this is the structure we fabricated and tested. However, the geometrical aberrations introduced by breaking the spherical symmetry with the adjustable fold mirror are reduced by scaling down the lens, and a shorter focal length is preferred for many mobile electronics applications; therefore, we also scaled the design to a 6-mm focal length for comparison.

B. Lens Designs

To better understand the trade-offs for the three focusing methods shown in Fig. 2, we modeled a 6- and 12-mm focal length lens with all three methods for the overall lens layout shown in Fig. 3. We varied the object distances between 0.5 and 100 m and adjusted either the focal surface position, piston shift of a flat mirror, or positive and negative curvature of a mirror with the center point fixed relative to the center of the meniscus lens. Figure 4 shows the resulting relationship between axial optomechanical displacement and object conjugate for the $f = 12$ mm lens. While the scale of the figure is specific to these particular optical designs, the trends between the focusing methods are applicable to all positive monocentric lenses of the types discussed in [5]. For both the 6- and 12-mm focal length designs, the required optomechanical actuation for a focal shift from 0.5 m to 100 m is about 30 times smaller for the mirror deformation method than standard axial displacement and 40 times smaller than for internal flat ‘piston’ shift.

To limit the required travel length of the actuator for compact systems, we concentrated on mirror focus deformation. The departure from monocentricity and the resulting aberrations are minimized using mirror deformation that varied from positive through negative curvature (push and pull of the mirror’s center), where a flat mirror focused to some intermediate object conjugate. For simplicity in the experimental demonstration, we considered unipolar actuation (positive curvature applied by push only) and found that the impact on resolution was modest (16% average reduction in MTF50 across all fields and object distances).

We used a minimal 12° fold angle in the design to reduce the $\cos \theta$ vignetting at the cost of a slightly thicker system. Notice that in the ray race (Fig. 3), the image surface clips

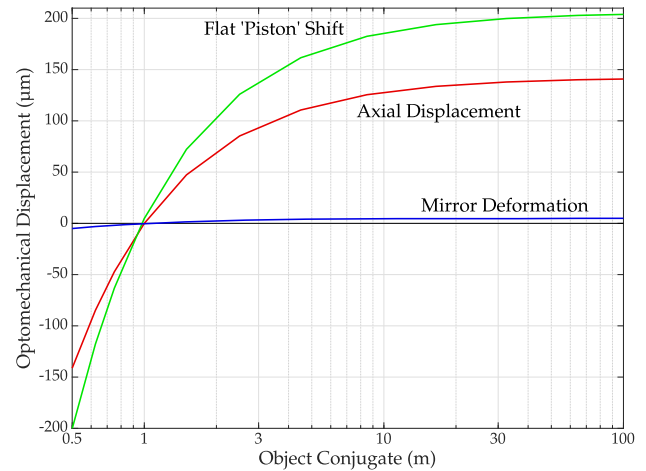


Fig. 4. Optomechanical displacement as a function of object conjugate distance (shown in logarithmic scale) of the 12-mm focal length lens for the three different focusing methods. The total linear actuator excursion for axial displacement of the focal surface is $284 \mu\text{m}$, for flat ‘piston’ piston shift of the fold mirror is $405 \mu\text{m}$, and for the maximum (central) excursion for a spherically deformed fold mirror is $9.9 \mu\text{m}$. The corresponding excursions for the $f = 6$ mm design (not shown) are $71 \mu\text{m}$, $102 \mu\text{m}$, and $2.5 \mu\text{m}$, respectively.

the edge of the vertical field, an intentional choice to balance the asymmetric vignetting from the folding of the lens. Figure 5 shows the resulting illumination of the designs without clipping.

The optical parameters of the final F/2.8 design are in Table 1. The radius of curvature of the fold mirror varied from -1.595 to $+1.627$ m. The modulation transfer function (MTF) performance plots are seen in the left column of Fig. 6 for horizontal FOV of $\pm 55^\circ$ and vertical FOV of $\pm 8^\circ$. If the lens were focused using traditional axial shift of the focal surface, it would achieve diffraction-limited performance with an average Strehl ratio of 0.97 for all object distances, like that seen for the 1.0 m object distance in the middle row of Fig. 6. Our tolerance analysis resulted in desired radial and decentration errors up to $\pm 5 \mu\text{m}$ and surface roughness R_a within 10 nm, which were within the specified limits

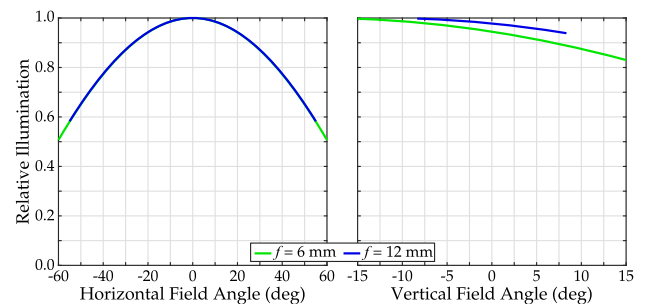


Fig. 5. Relative illumination plots of the horizontal (left) and vertical (right) field angles for both folded monocentric lens designs. Notice the asymmetric vignetting along the vertical fields caused by the folding of the lens.

Table 1. Optical Parameters of the $f = 12$ mm Lens

Surface	Radius	Thickness	Material	Semidiameter
1	6.138164	3.092915	POLYSTYR	5.670209
2	3.045250	Variable	CARG0608	2.928836
3	Variable	n/a	MIRROR	1.5

for the single point diamond turned element that will be described in Section 4. Note that the prototype was assembled with a 25° fold angle to prevent mechanical interference of the stock optical mounts.

To design the 6 mm focal length lens, we used the same design constraints in fold angle, $F/\#$, materials, and tolerances. The radius of curvature required to focus this lens does not change. The reduced optical aberrations in the down-scaled lens allowed us to maintain near diffraction-limited MTF while extending both the horizontal and vertical fields-of-view. The resulting optical parameters of the final $F/2.8$ design are in Table 2, and MTF plots for horizontal FOV of $\pm 60^\circ$ and vertical FOV of $\pm 15^\circ$ are found in the right column of Fig. 6.

3. FOCUS MIRROR ACTUATION

The folded imager can be focused by applying a spherical (paraxially quadratic) phase profile on the central reflector. This phase profile can, in general, be applied by an electro-optic modulator or liquid-crystal-on-silicon (LCOS) display, and such devices may also apply higher order aberration correction. However, the total excursion for the 12-mm focal length lens of $10 \mu\text{m}$ (approximately 20 waves) exceeds the range of most modulators, which means that the phase profile would be displayed modulo $2\pi N$, yielding some degree of chromatic aberration and energy into higher diffraction orders. A mechanically deformed mirror might use microfluidic, electromagnetic, or piezoelectric actuation to provide an optically continuous surface over the full range needed. Piezoelectric actuators have high resolution and can be compact, both ideal characteristics for this system. Longitudinal piezo actuators provide only some 0.1% to 0.15% displacement of the actuator length, but this can be enhanced by lever amplification. Bending actuators provide translation factors of 30 to 40 \times . Both unimorph and bimorph piezoelectric deformable mirrors with four or more contacts have been used for low-cost and low-order aberration

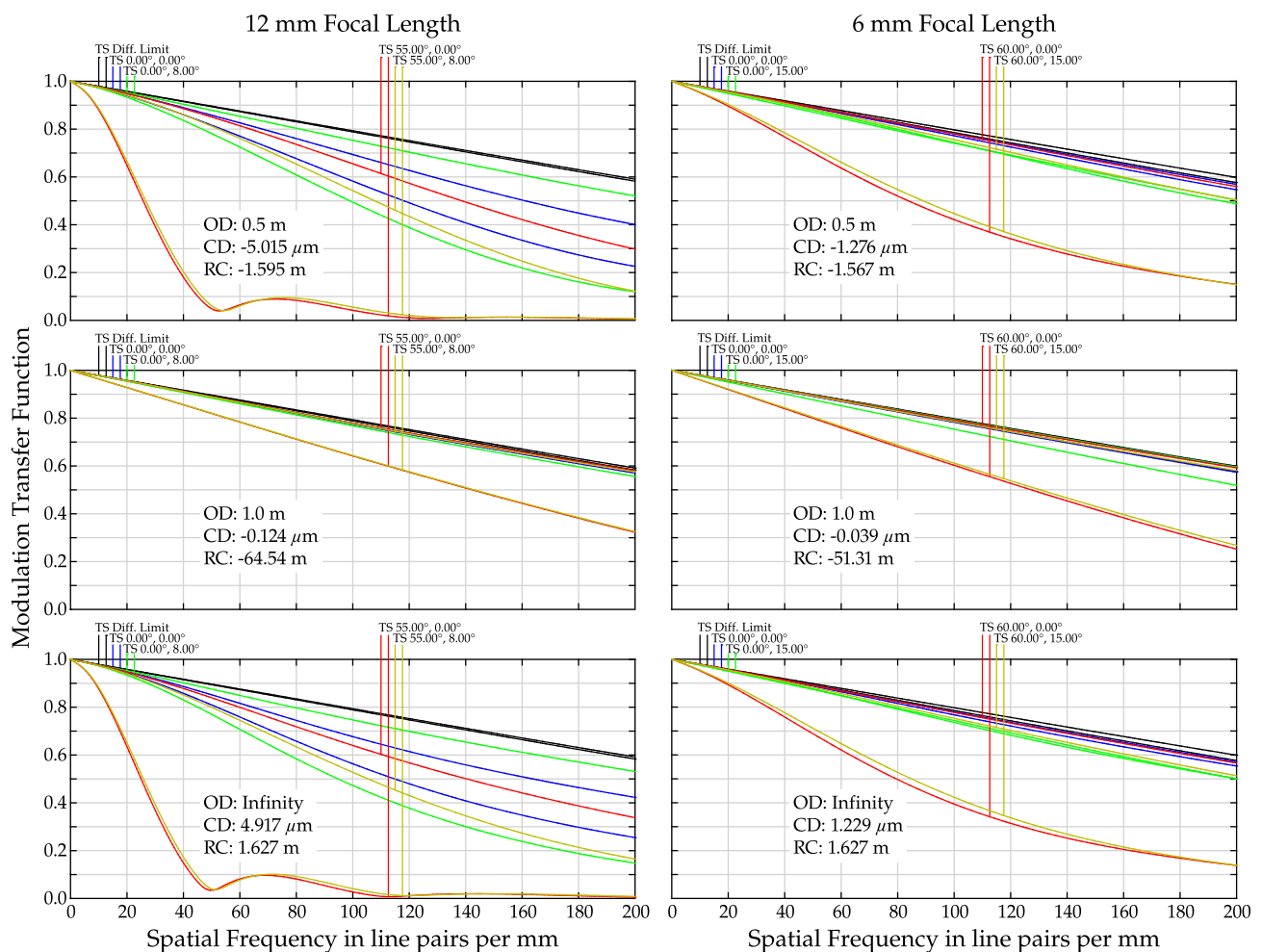


Fig. 6. MTF plots of the $f = 12$ mm (left column) and the $f = 6$ mm (right column) folded monocentric lenses with fully variable mirrors at object distances (OD) of 0.5 m (top), 1.0 m (middle) and infinite (bottom) object distances. The center displacement (CD) and radius of curvature (RC) of the fold mirror are shown for each configuration. Scans across the tangential (T) and sagittal (S) planes for various field angles are labeled above the plots.

Table 2. Optical Parameters of the $f = 6$ mm Lens

Surface	Radius	Thickness	Material	Semidiameter
1	3.070166	1.546019	POLYSTYR	2.936707
2	1.524147	Variable	CARG0608	1.492035
3	Variable	n/a	MIRROR	0.76

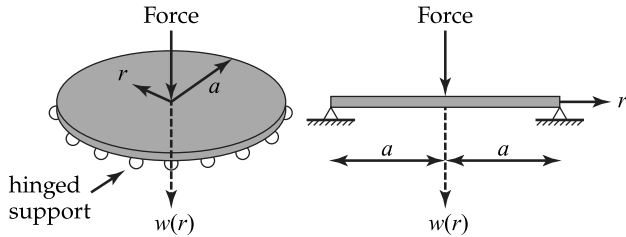


Fig. 7. Diagram of hinged circular plate under central point load.

correction for adaptive optics [11,12], and spherical focus may be applied with as little as two electrical contacts.

The focus mechanism we chose to investigate in this paper is a mechanically actuated deformable mirror system: an edge-supported circular mirror plate under central point contact with a mechanical actuator, as shown in Fig. 7. Bidirectional force can be applied by a voice coil actuator, and unidirectional force can be applied by a small stepper motor driving an eccentric cam. The latter would be a scaled-down version of the arrangement used to translate and focus the monocentric lens in [6]. Such push only mirror deformation can be modeled as a hinged elastic circular plate under a central point load, as described in [13]. For such a plate shown in Fig. 7 the deformation is

$$w(r) = w_0 \left[\left(1 - \frac{r^2}{a^2} \right) + 2 \left(\frac{1 + \nu}{3 + \nu} \right) \left(\frac{r}{a} \right)^2 \log \left(\frac{r}{a} \right) \right], \quad (1)$$

where w_0 is the center displacement (dependent on material properties, geometry, and force applied) and ν is Poisson's ratio for the material. This RMS error of this model from spherical for borosilicate glass ($\nu = 0.206$) across the 3-mm diameter open aperture of the 12-mm focal length lens design is 38.5 nm for a 5 μm center displacement (maximum for a push-pull system) and 77.0 nm for a 10 μm center displacement (maximum for a push only system). We extended this model to allow for asymmetric curvature by making the radially symmetric Eq. (1) bivariate in x and y with independent coefficients for the two axes.

To quantify the optical profile response of such a deformable mirror, we constructed an experimental system with the mirror exposed and then measured the surface deformation developed with a white light interferometric profilometer (Veeco NT1100). We placed an aluminum-coated circular borosilicate microscope cover glass, which was 9 mm in diameter and 145 μm thick, against an annular steel shim spacer with an inner and outer diameter of 7.24 mm and 9.53 mm, respectively. This contact enforces the hinged boundary condition. We then applied the spherical tip of a precision differential micrometer at the center of the mirror substrate. Figure 8 shows the resulting scan of the mirror at minimum and maximum deformation

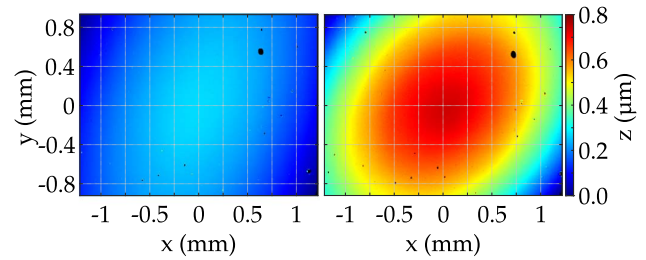


Fig. 8. White light interferometric scans of custom mirrors before deformation (left) and after maximum deformation (right) to achieve full range of focus.

for the full range of focus for the prototype system of Section 4. The deformation is approximately spherical, except that there is a clearly visible asymmetry (astigmatism) in the elliptical phase profile.

We fit the bivariate form of Eq. (1) to the interferometric scans using the center displacement w_0 , Poisson's ratio ν , and the radius of the hinge a as the variable parameters. We also performed an additional 5th order polynomial fit to the residual error to correct for the remaining discrepancies between the measured scan and model. The resulting model and final error from measurement are shown in Fig. 9.

The source of the asymmetry was the imperfect flatness of the annular spacer, which enforced the hinged boundary condition. We measured the linear variation of the spacer from flat across the 7.24-mm inner diameter to be as much as 0.5%, more than sufficient to explain the 0.01% observed for the maximally deformed mirror across the measured 3.5 mm diameter. The thickness of the spacer only varied about 0.05% of the inner diameter, suggesting that the variation from flat was caused by cylindrical curvature imparted during fabrication. We measured several sample spacers and found that all exhibited similar variations. In the absence of a flatter spacer, we proceeded to integrate this modulator into the optical

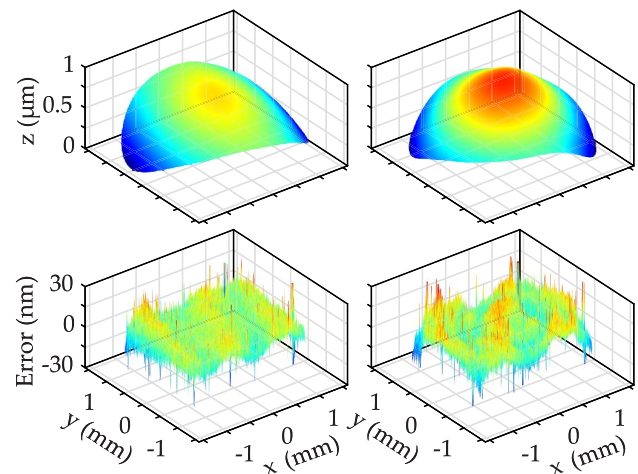


Fig. 9. Fit of interferometric scan data to hinged plate model with 5th order polynomial correction to residuals (top row) and the remaining error between model and measured data (bottom row). The mirror before and after maximum deformation to achieve full range of focus are shown in the left and right columns, respectively.

system described in Section 4, noting that the asymmetry will cause astigmatism in the resulting images, but that the measured phase profile can be used to model and understand the measured resolution.

4. PROTOTYPE SYSTEM

A. Lens Assembly

The 12-mm focal length rigid meniscus lens was fabricated by ISP Optics with direct single point diamond turning of optical grade polystyrene, without post polishing. Their process yielded specular surfaces with outer and inner surface roughness R_a of 7.7 and 4.5 nm. The decentration of the optical surfaces to the handle was less than 7 μm , and the inner and outer radii of curvature departed by 0.2 and 4.3 μm from the corresponding designs of 6.1382 and 3.0453 mm. The 5.9-mm diameter optical region of the back side of the lens was surrounded by a recess for the precision spacer and deformable mirror, set into a rough-surfaced mechanical handle for mounting in a standard 20 mm benchtop lens ring mount. We fabricated the mirror for the folded monocentric imager by cutting No. 1 (0.13 to 0.16 mm thick) borosilicate microscope cover glass into a 9-mm diameter disk, upon which we sputtered an aluminum mirror. The aperture stop was implemented by punching an annulus with 3.2 and 9.3 mm inner and outer diameters into 0.157-mm thick high density paper-based blackout tape and applying the ring-shaped filter to the aluminum-coated cover glass disk.

We assembled the folded lens (Fig. 10) using a pneumatic dispensing syringe to deposit approximately 50 μL of optical gel (Cargile 0608), degassed to remove trapped air bubbles, into the core of the polystyrene element. This volume of the high viscosity gel is sufficient to make complete contact with the entire open aperture area, while leaving a peripheral air cavity that can compress and expand during mirror deformation. We placed the steel shim spacer in contact with the lens recess to provide the static radial fulcrum for the deformation, and then brought the mirror into contact with the convex surface of the

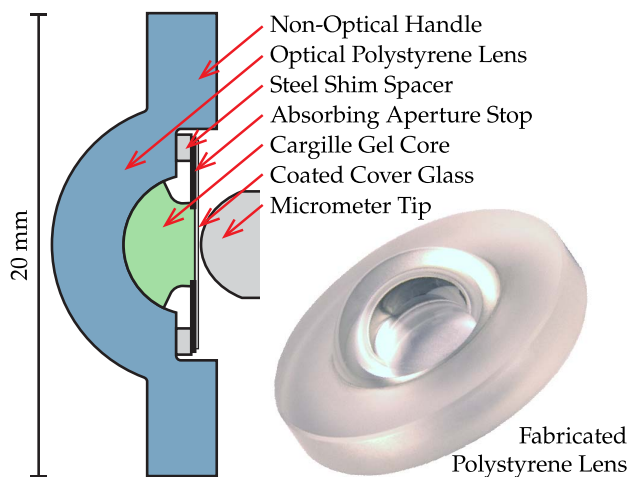


Fig. 10. To-scale cross-sectional diagram of assembled $f = 12$ mm lens with deformable mirror focusing through micrometer actuation and inset photo of fabricated outer lens.

gel, minimizing bubbles, and maintaining the annular air cavity. The assembled optics were mounted vertically, and the rear of the deformable mirror placed in contact with a spherical tipped precision differential micrometer with a resolution of 0.5 μm per readable division. This actuator was centered prior to lens assembly by looking at the reflection of an alignment laser off of the spherical reflective tip of the actuator. We estimate the positioning centration error to be less than 25 μm (which is less than 0.5% of the mirrors 7.24 mm diameter of the bending region). This applies positive curvature (push only) in combination with a small piston shift (as the center of the mirror moves axially unlike the right most diagram in Fig. 2), allowing for a proof-of-principle demonstration. The surface tension of the gel was sufficient to hold the mirror in place during mounting, and there was no indication of an internal misalignment during the weeks-long course of the experiments.

B. Imaging System Characterization

We built the test system shown in Fig. 11 to allow two methods of capture of the spherical image surface: first by a high-resolution microscope to relay a small region of the image formed to probe the capabilities of the lens itself, then using one of the FC CMOS sensors shown in Fig. 1(a) from [6] to demonstrate resolution achievable with a self-contained image sensor. We constructed a test scene from four United States Air Force (USAF) resolution test targets placed at 0.5, 1.0, 2.0, and 3.0 m and positioned the image capture element (relay or FC sensor) to focus onto the closest test object with minimum mirror deformation. This allowed us to compensate for any error in the axial position of the mirror with respect to the center of curvature. We captured an image for each adjustment of the micrometer over a sweep through the focal range of the system.

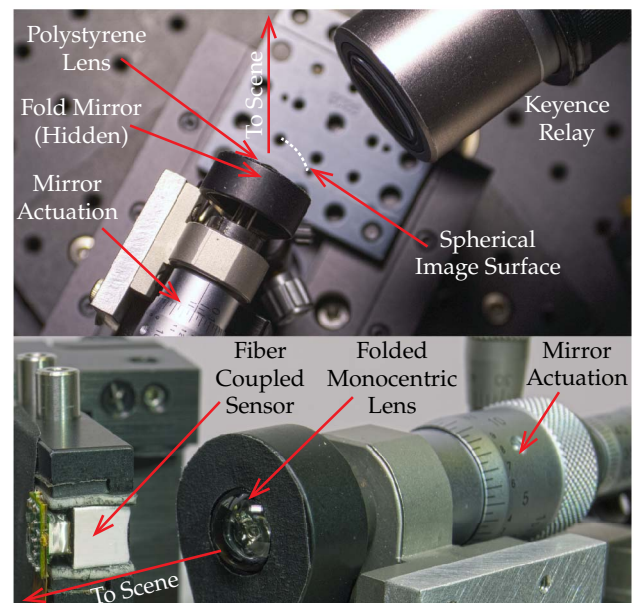


Fig. 11. Photos of the $f = 12$ mm lens and differential-micrometer driven deformable mirror from above and configured to image with the optical relay (top) and from the front when configured to image with the FC image sensor (bottom).

The microscope used to inspect the image was a Keyence VHX-1000 with a VH-Z100UR zoom lens, which, when set at 300× (6× optical magnification), provided a 0.19 numerical aperture and 8.46° full FOV when imaging through the monocentric lens onto the 1/18" CCD. The FC image sensor, described in more detail in [6], uses a Schott fiber optics 24AS faceplate with 2.5 μm fiber core pitch that is polished to a 12 mm radius of curvature on the input face and flat on the rear surface. The input of a single sensor captures a 22° by 16° full FOV of the curved sub-image, one region of the 110° wide letterbox panorama that can be captured with a row of five such sensors. The fiber bundle is coupled to the CMOS sensor with a 2 μm adhesive seam between the rear surface of the fiber bundle and the Bayer filters of a OmniVision 5653 sensor with 1.75 μm pitch pixels. This FC image sensor provides a compact measurement of the curved wide-angle image surface but limits the spatial resolution to the 2.5 μm pitch of the fiber bundle, at best. We used a fold angle of 25° (50° full angle) to allow for clearance of the monocentric lens mount.

We began by capturing images using the Keyence relay, such as those in Fig. 12. Actuation of the micrometer deformed the mirror and shifted the focus from the resolution test chart at 0.5 m to the chart at 3.0 m, successfully demonstrating refocus. We modified the scene to extend over the wider FOV FC sensor, 22° compared to the relay's 8.35°. Note that to allow direct comparison of resolution measurements for both sensors,

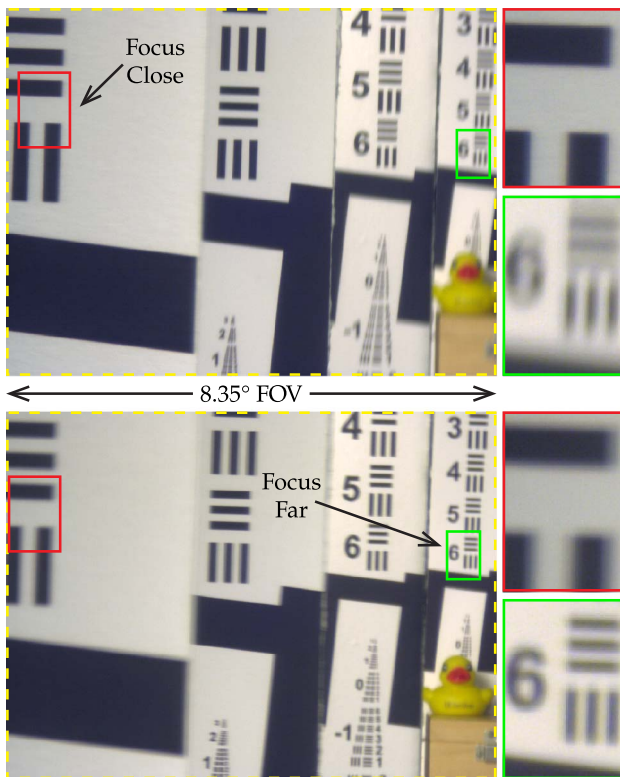


Fig. 12. Images captured through the Keyence image relay using the $f = 12$ mm lens with deformable mirror focus. The top and bottom images are focused to 0.5 and 3.0 m OD, respectively, with inset regions of interest.

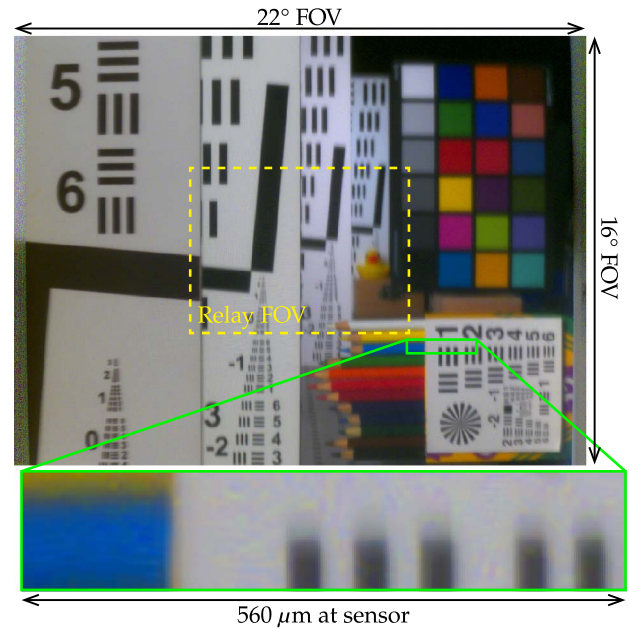


Fig. 13. Fully processed photo captured through FC sensor when focused to 1 m with a magnified inset. The relative FOV of the images captured through the Keyence image relay (2.6× magnification) is shown in the yellow dashed box.

the images were taken using identical object distances and field angles. We processed the images from the FC sensor using flat field correction, Malvar-He-Cutler Bayer demosaicing [14], color matrix correction, and white balancing, at which point we measured the MTF. To aesthetically enhance the final images we applied gamma correction, C-BM3D noise reduction [15], and unsharp masking to produce the image shown in Fig. 13.

We deformed the mirror to sweep the focus of the system in the regime surrounding the point of best focus and recorded the point spread function (PSF) to generate a through-focus PSF measurement that is shown in the top row of Fig. 14. This

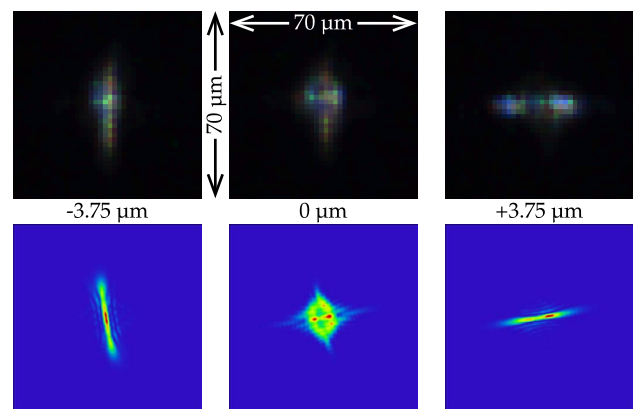


Fig. 14. Through-focus PSF measurement with FC sensor (top) and simulation using scanned mirror (bottom) of the $f = 12$ mm lens. The change in focus was obtained by translating the micrometer deforming the mirror.

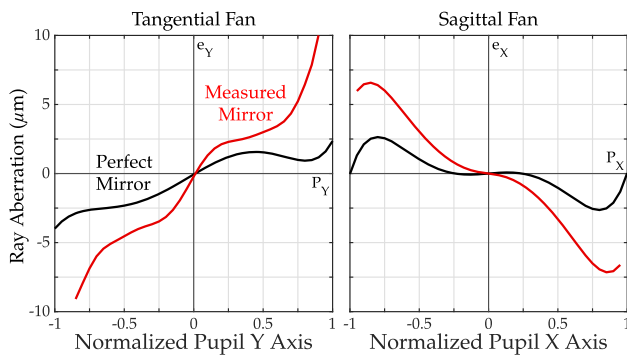


Fig. 15. Simulated on axis transverse ray fans at a 1.0 m object distance. The larger slope discrepancy between the tangential and sagittal planes for the mirror as measured (red) as opposed to spherical (black) indicates an increase in astigmatism.

allows us to observe the generated impulse response as it transforms around the optimal focal position, revealing aberrations. The dominant aberration is astigmatism, clearly visible in the transition from horizontal to vertical confinement in the PSFs as well as the transverse ray aberration plot in Fig. 15. This is apparently a consequence of non-rotationally-symmetric deformation of the mirror by the non-uniform spacer. To check whether this image aberration was consistent with the measured mirror profile, we updated the “ideal” lens design by replacing the spherical focus mirror with an imported extended polynomial mirror in Zemax. This imported surface was a 14th order polynomial fit to the bivariate plate deformation model based on the interferometric measurements at various deformation amounts described in Section 3. We used rotation as the degree of freedom to align the astigmatism axes

and simulated the output PSFs shown in the bottom row of Fig. 14, which are consistent with the experimental results.

To clarify the impact of the astigmatism, the simulated and measured MTF plots in Fig. 16 are shown for both the best overall focus (defined when the sagittal and tangential resolution are equal) as well as the best tangential focus to show the capability of the lens if only the mirror deformed symmetrically. The MTF for the best sagittal focus was similar to the MTF for the best tangential focus. When using the image relay, the system achieved an average MTF50 of 52.6 lp/mm at the best focus and 99.0 lp/mm at the best tangential focus for all object distances. The similarity between the measurement and the simulation when using the interferometric mirror scan and their difference to the simulation with the perfect mirror indicate that the asymmetry in the deformation of the mirror dominated the loss in resolution. To quantify the loss in resolution from fiber coupling, Fig. 17 shows the MTF plots when using the FC sensor for best overall and tangential focus for 1.0 through 3.0 m object distances. When using the FC sensor the system achieved 23.7 and 32.0 lp/mm MTF50 for the two focusing conditions.

The total required micrometer displacement to focus between objects was 9.0 μm and 4.7 μm for the relay and FC sensor, respectively, compared to the simulated 3.3 μm . The larger than expected translation required to sweep the focus when capturing with the relay as compared to the FC sensor is likely due to the additional refocusing required to capture the curved image with the flat image sensor of the Keyence microscope. There may have also been compression and/or flexure of the lens and mounts when the micrometer was adjusted, which could have caused the mirror to slightly shift axially while curving, blending the piston shift and curvature focusing (an effect observed when interferometrically scanning the mirror in Section 3).

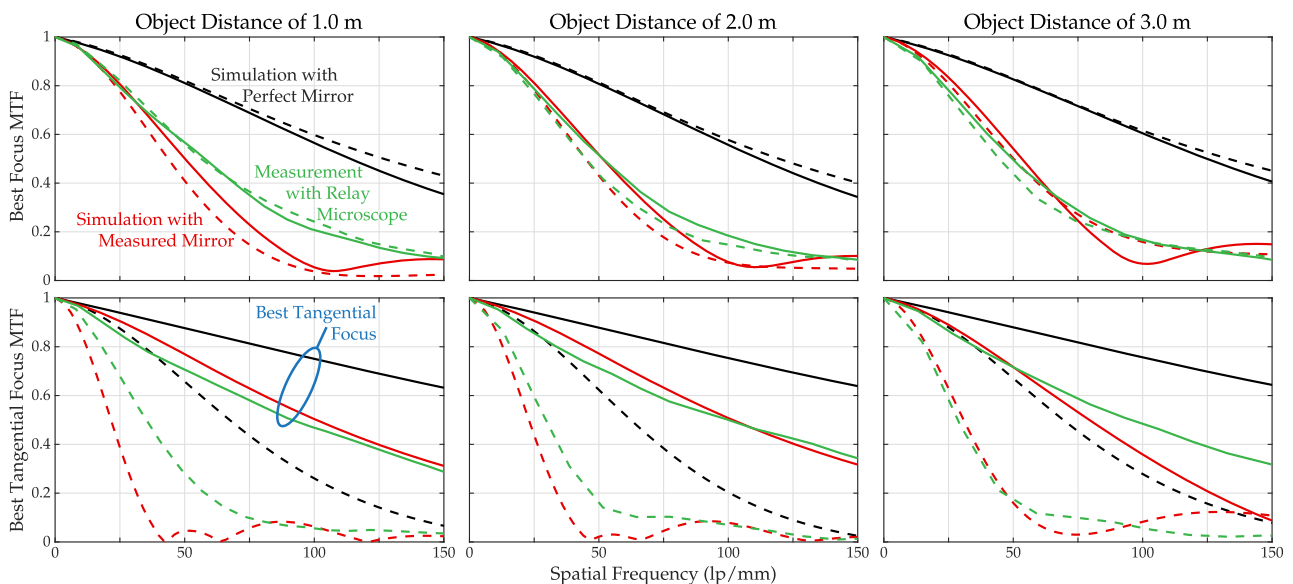


Fig. 16. Optical relay MTF measurements (green) of the $f = 12$ mm lens with deformable mirror focused at various OD. The corresponding Zemax simulated resolution using the polynomial fit to the measured interferometric data (red) and with a perfect spherical mirror (black) are also shown. The solid and dashed lines are tangential and sagittal rays, respectively, and the relay microscope limited Nyquist frequency from the 1.1 μm pitch pixels (including optical magnification) is 455 lp/mm.

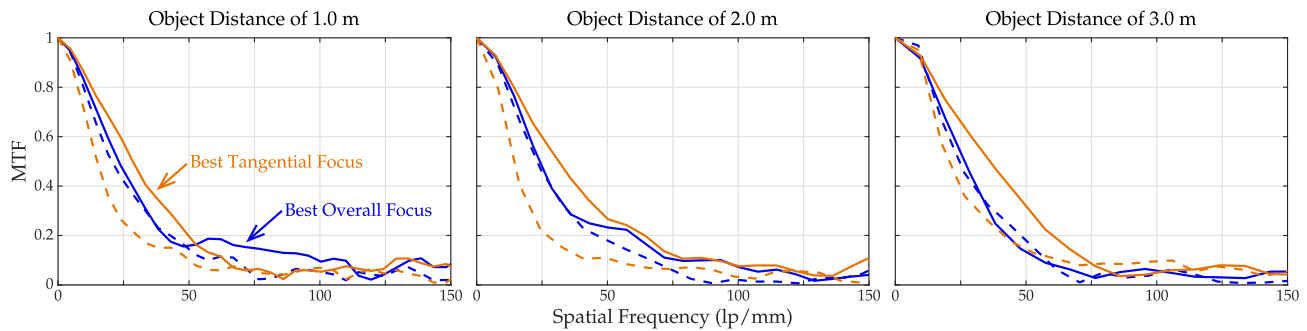


Fig. 17. FC sensor MTF measurements of the $f = 12$ mm lens with deformable mirror focused at various OD. The blue lines represent the best overall focus, and the orange lines show the best tangential focus. The solid and dashed lines are tangential and sagittal rays, respectively, and the fiber limited frequency from the quasi-periodic $2.5 \mu\text{m}$ fiber pitch is 200 lp/mm.

5. CONCLUSION

We have defined a new configuration for nearly-monocentric imaging wherein the monocentric lens is folded at the center of symmetry and focused by applying spherical deformation (optical power) to the fold mirror. The folded configuration provides a more compact layout, especially if the layout incorporates a secondary fold mirror. Such layouts restrict the vertical FOV, but they still support a wide (120° or larger) horizontal FOV. Focusing with internal spherical deformation breaks the strict monocentric symmetry and reduces the resolution of the imager at the near and far conjugates, especially in the longer focal length design. The key advantage of the folded geometry is size. In addition to the lens layout, focus by spherical deformation requires $30 \times$ less mechanical excursion than by sensor translation, making this geometry compatible with highly compact optomechanical actuators, such as bimorph piezoelectric deformable mirrors.

We fabricated and tested a 12-mm focal length prototype focused by mechanical deformation of a thin fold mirror. Image resolution was limited by astigmatism from the mirror mounting, but the system still provided proof-of-principle for the new focus layout. When the measured fold mirror aberrations were incorporated into the lens model, the design closely followed the experimental results. The system was operated with a single FC image sensor, and the extension to wide-angle imaging with a linear array of such sensors is straightforward.

Looking forward, the next step would be to integrate a higher quality fold mirror with a compact focal actuator and an image sensor capable of resolving the full FOV. The FC image sensor is limited by the current $2.5 \mu\text{m}$ fiber pitch, and it cannot resolve 200 lp/mm or higher resolutions possible with the 6-mm focal length design. However, spherical CMOS image sensors are the subject of on-going research and development [16,17], and it may become practical to provide a high resolution directly-illuminated CMOS sensor. Access to the monocentric lens pupil in this folded design may also allow integration of a variable aperture, either mechanical, electrowetting [18], or dielectric [19]. Folded monocentric imagers do provide a promising design option to satisfy the desire for wider fields-of-view in smaller package sizes that are present in many of today's imaging applications.

Funding. Google's Advanced Technology and Projects Group (20141325).

REFERENCES

1. H. Ren, D. Fox, P. A. Anderson, B. Wu, and S. T. Wu, "Tunable-focus liquid lens controlled using a servo motor," *Opt. Express* **14**, 8031–8036 (2006).
2. H. Ren and S. T. Wu, "Variable-focus liquid lens by changing aperture," *Appl. Phys. Lett.* **86**, 211107 (2005).
3. S. W. Lee and S. S. Lee, "Focal tunable liquid lens integrated with an electromagnetic actuator," *Appl. Phys. Lett.* **90**, 121129 (2007).
4. S. Y. Lee, H. W. Tung, W. C. Chen, and W. Fang, "Thermal actuated solid tunable lens," *IEEE Photon. Technol. Lett.* **18**, 2191–2193 (2006).
5. I. Stamenov, I. P. Agurok, and J. E. Ford, "Optimization of two-glass monocentric lenses for compact panoramic imagers: general aberration analysis and specific designs," *Appl. Opt.* **51**, 7648–7661 (2012).
6. I. Stamenov, A. Arianpour, S. J. Olivas, I. P. Agurok, A. R. Johnson, R. A. Stack, R. L. Morrison, and J. E. Ford, "Panoramic monocentric imaging using fiber-coupled focal planes," *Opt. Express* **22**, 31708–31721 (2014).
7. S. Karbasi, I. Stamenov, N. Motamedi, A. Arianpour, A. R. Johnson, R. A. Stack, C. LaReau, R. Tenill, R. Morrison, I. P. Agurok, and J. E. Ford, "Curved fiber bundles for monocentric lens imaging," *Proc. SPIE* **9579**, 95790G (2015).
8. J. M. Cobb, "Autostereoscopic desktop display: an evolution of technology," *Proc. SPIE* **5664**, 139–149 (2005).
9. D. Shafer, "Some odd and interesting monocentric designs," *Proc. SPIE* **5865**, 56–66 (2005).
10. R. N. Wilson, *Reflecting Telescope Optics I: Basic Design Theory and its Historical Development* (Springer, 2007).
11. J. C. Dainty, A. V. Koryabin, and A. V. Kudryashov, "Low-order adaptive deformable mirror," *Appl. Opt.* **37**, 4663–4668 (1998).
12. J. Ma, Y. Liu, T. He, B. Li, and J. Chu, "Double drive modes unimorph deformable mirror for low-cost adaptive optics," *Appl. Opt.* **50**, 5647–5654 (2011).
13. J. N. Reddy, *Theory and Analysis of Elastic Plates and Shells* (CRC Press, 2006).
14. H. S. Malvar, L. W. He, and R. Cutler, "High-quality linear interpolation for demosaicing of bayer-patterned color images," in *IEEE International Conference on Acoustics, Speech, and Signal Processing* (IEEE, 2004), Vol. **3**, pp. iii–485.
15. K. Dabov, A. Foi, V. Katkovich, and K. Egiazarian, "Image denoising by sparse 3-D transform-domain collaborative filtering," *IEEE Trans. Image Process.* **16**, 2080–2095 (2007).
16. T. Wu, S. S. Hamann, A. C. Ceballos, C. E. Chang, O. Solgaard, and R. T. Howe, "Design and fabrication of silicon-tessellated structures for monocentric imagers," *Microsyst. Nanoeng.* **2**, 16019 (2016).

17. K. Itonaga, T. Arimura, K. Matsumoto, G. Kondo, K. Terahata, S. Makimoto, M. Baba, Y. Honda, S. Bori, T. Kai, K. Kasahara, M. Nagano, M. Kimura, Y. Kinoshita, E. Kishida, T. Baba, S. Baba, Y. Nomura, N. Tanabe, N. Kimizuka, Y. Matoba, T. Takachi, E. Takagi, T. Haruta, N. Ikebe, K. Matsuda, T. Niimi, T. Ezaki, and T. Hirayama, "A novel curved CMOS image sensor integrated with imaging system," in *Symposium on VLSI Technology (VLSI-Technology): Digest of Technical Papers* (IEEE, 2014), pp. 1–2.
18. L. Li, C. Liu, H. Ren, and Q. H. Wang, "Adaptive liquid iris based on electrowetting," *Opt. Lett.* **38**, 2336–2338 (2013).
19. C. G. Tsai and J. A. Yeh, "Circular dielectric liquid iris," *Opt. Lett.* **35**, 2484–2486 (2010).